Climatic Change (2026) 179:99
https://doi.org/10.1007/s10584-026-04192-7

RESEARCH ARTICLE

Reduced annual temperature cycle amplitude over the high-elevation Tibetan Plateau induced by black carbon aerosols

Lihua Zhu[1] · **Wei Hua**[1] · **Gang Huang**[2,3] · **Xin Lai**[1]

Received: 11 April 2025 / Accepted: 20 April 2026

Abstract
The Tibetan Plateau harbours the largest ice mass outside the polar regions and supports abundant biodiversity. The annual temperature cycle profoundly influences both the cryosphere and biosphere. However, the mechanisms underlying the changes in the annual temperature cycle over the Tibetan Plateau under global warming remain poorly understood. The present study documents the changes in the amplitude of the annual temperature cycle over the Tibetan Plateau and examines their physical association with black carbon (BC) aerosols. We report a decrease in the amplitude of the annual temperature cycle over the Tibetan Plateau in recent decades, with the most pronounced negative trends occurring at elevations of 4000–5300 m ($p<0.05$). Detection and attribution analysis attributes this intensified weakening of the annual temperature cycle amplitude on the high-elevation Tibetan Plateau primarily to anthropogenic activities, particularly aerosols. BC-induced albedo darkening plays a crucial role in winter. Statistical analysis and numerical modelling reveal that increasing BC aerosols over the Tibetan Plateau intensify winter surface warming by darkening the surface and exerting positive direct radiative forcing. More importantly, the most robust sensitivity of the winter surface air temperature to the change in BC aerosols occurs at higher elevations on the Tibetan Plateau, where greater aged snow depths persist with limited fresh snowfall, maintaining larger grain sizes. Consequently, the intensification of winter warming by BC aerosols has decreased the annual temperature cycle amplitude over the high-elevation Tibetan Plateau. These findings are crucial for interpreting the changes in the annual temperature cycle over the Tibetan Plateau and for constraining predictions about the future of the cryosphere and biological diversity.

Keywords Annual temperature cycle amplitude · High-elevation Tibetan Plateau · Black carbon aerosols · Albedo darkening

Extended author information available on the last page of the article

Published online: 27 April 2026

1 Introduction

Global warming is an indisputable fact. In addition to an increase in the mean temperature, a warming climate consequently affects the cryosphere (Shepherd et al. 2018), ecosystems (Richardson et al. 2018), species (Steinbauer et al. 2018), agriculture (Zhu et al. 2022), etc. One of the key factors influencing these climatic effects is the change in the annual temperature cycle (ATC). An ATC with a warmer winter reduces the temperature fluctuation below the freezing point, increases the number of days with air temperatures varying around the freezing point, and results in the dominance of white ice before ice-off (Weyhenmeyer et al. 2022) and variations in precipitation type (Jennings et al. 2018). The ATC over extratropical land has shifted towards earlier seasons (Stine et al. 2009), which results in earlier melting of snowpack (Hamlet et al. 2005), a decreased duration of the frozen season per year (Kim et al. 2012), and a decreased snow cover extent and duration in the Northern Hemisphere (Hori et al. 2017; Choi et al. 2010). The ATC is also critical for simulating the evolution of ice sheets and interpreting glacial landforms and chronologies (Buizert et al. 2018). The amplitude of the ATC can increase the early thaw rates of permafrost (McKenzie and Voss 2013) and profoundly affects water transport, ice table depth, ground ice content and permafrost stability in icy permafrost soils (Fisher et al. 2016, 2020). Additionally, changes in the ATC can affect biological and ecological systems, such as biological growth (Vicente Liz et al. 2019), species distributions (Zhao et al. 2021) and richness (Shrestha et al. 2018), plant developmental genetics (Li et al. 2010), and insect physiological traits (Bujan et al. 2020).

As the Third Pole and roof of the world, the Tibetan Plateau (TP) has the largest store of ice outside the polar region (Qiu 2008) and hosts a wide variety of species including both animals and plants (Cheng et al. 2023; Mao et al. 2021). Although it is essential to interpret the variation in the ATC to better understand climate change over the TP and its climatic effects on the cryosphere and biosphere, studies on the variation in the ATC over the TP and its causes are lacking. Like the amplitude of the ATC over land in extratropical locations in the Northern Hemisphere (Duan et al. 2019; Stine et al. 2009; Wang and Dillon 2014), a significant change has also been observed over the TP (Duan et al. 2017). However, a key knowledge gap exists regarding the cause of the decreasing ATC over the TP, and a more detailed mechanistic understanding is needed. Snow albedo feedback is an important positive feedback that is crucial over the snow-dominated TP in winter. Aerosols transported from heavily polluted regions around the TP can enter the environment, impacting the cryosphere by darkening the surface and accelerating melting (Di Mauro 2020; Kang et al. 2019; Li et al. 2016; Sarangi et al. 2020). The transport and deposition of aerosols clearly show a seasonal cycle with a maximum during the non-monsoon period and a minimum in the monsoon period (Kang et al. 2019; Wan et al. 2017; Zheng et al. 2020). BC aerosols have been considered a significant contributing factor to cryospheric changes (Kang et al. 2020; Niu et al. 2017; Xu et al. 2009). A key but poorly quantified mechanism is that BC may increase winter warming via the snow–albedo feedback, thereby potentially weakening the ATC amplitude. This leads directly to our central research question: How do anthropogenic aerosols, especially BC, drive the observed weakening of the ATC amplitude over the high-elevation TP?

Here, using gridded observational datasets, satellite observations, reanalysis data, and outputs from the Coupled Model Intercomparison Project Phase 6 (CMIP6) of the World Climate Research Program, we investigate the drivers of the robust decrease in the ATC

amplitude over the high-elevation TP. In particular, we examine the role of anthropogenic aerosol forcing and the associated processes involving surface albedo changes and radiative effects. This analysis is important for interpreting the changes in the ATC over the TP and for constraining predictions about the future of the cryosphere and biodiversity.

2 Data and methods

2.1 Observational and reanalysis datasets and related analysis methods

2.1.1 ATC amplitude

Daily surface air temperature (SAT) data from gridded observational datasets provided by the National Climate Center of the China Meteorological Administration (CN05.1; Wu and Gao 2013) were used to investigate and evaluate the changes in the ATC amplitude. The datasets are available at a 0.25°×0.25° spatial resolution. The dataset version used in this study covers 1961–2020. CN05.1 has been widely used to analyse regional climate change and validate climate models (Shi et al. 2018; Wu et al. 2017), as well as to investigate elevation-dependent warming over the TP (Niu et al. 2021).

The ensemble empirical mode decomposition (EEMD; Wu and Huang 2009) method, a temporally local and adaptive filter, was applied to isolate the annual cycle (Qian et al. 2011; Qian and Zhang 2015; Wu et al. 2008) and subsequently estimate the contribution of the ATC to the total variance in the monthly SAT over the TP. The seasonal maximum SAT over the TP occurs in summer (June–July–August, JJA) and the minimum occurs in winter (December–January–February, DJF; Fig. S1). Therefore, a simplified scheme from the literature (Qian and Zhang 2015) was considered to estimate the amplitude of the ATC, the details of which are as follows:

$$\mathrm{A} = \left(\mathrm{T_{JJA}} - \mathrm{T_{DJF}}\right)/2 \tag{1}$$

where A is the amplitude of the ATC, and T_{JJA} and T_{DJF} are the temperatures of the current JJA and the following DJF, respectively.

2.1.2 BC aerosol and radiation flux

The BC surface mass concentration, surface net downward shortwave flux assuming a clear sky, and surface net downward shortwave flux assuming a clear sky and no aerosols from the Modern-Era Retrospective Analysis for Research and Applications version 2 (MERRA-2) reanalysis data were used here. The MERRA-2 reanalysis product has relatively good temporal and spatial resolution, is available at 0.5°×0.625°, and spans 1980–present (Gelaro et al. 2017). It can accurately depict the spatiotemporal variability in absorbing aerosol species and has been widely utilized to investigate the distribution and long-term changes in regional aerosols (Buchard et al. 2015; Liu et al. 2019, 2022), such as those in high mountain regions (Feng et al. 2020; Sarangi et al. 2020). Moreover, surface aerosol direct radiative forcing was estimated here as the net radiation flux at the surface for clear skies

with aerosols minus that for aerosol-free clear air (Antón et al. 2011). We used data from this dataset covering 1981–2020.

2.1.3 Surface albedo

The Global Land Surface Satellite (GLASS; Liang et al. 2013, 2021; Liu et al. 2013) program provides a long-term (1981–2020), continuous, and high-spatial-resolution surface albedo product, with an accuracy comparable to that of the Moderate Resolution Imaging Spectroradiometer (MODIS) albedo product (He et al. 2013, 2014; Liu et al. 2013). We used the 1981–2020 data from this dataset. The GLASS satellite albedo product, which is consistent with ground-based observations over the TP (An et al. 2020; Chen et al. 2015), has been widely used in studies related to surface albedo over the region (e.g. Chen et al. 2022; Jiang et al. 2020; Miao et al. 2024). We calculated the surface albedo by combining the black-sky albedo (BSA) and white-sky albedo (WSA) from the GLASS shortwave radiation product. To achieve this, the monthly surface downward shortwave radiative flux (D_s) and surface direct shortwave radiative flux (D_{dir}) from the fifth-generation atmospheric reanalysis of the European Centre for Medium Range Weather Forecasts (ERA5) at 0.25°×0.25° were used to calculate the diffuse skylight ratio (F_{dif}):

$$\mathrm{F_{dif}} = \left(\mathrm{D_s} - \mathrm{D_{dir}}\right)/\mathrm{D_s} \tag{2}$$

The blue-sky albedo of the surface (ALB) can be derived as follows (Ma et al. 2019; Román et al. 2010):

$$\mathrm{ALB} = \left(1 - \mathrm{F_{dif}}\right) \times \mathrm{BSA} + \mathrm{F_{dif}} \times \mathrm{WSA} \tag{3}$$

2.1.4 Snowfall

Daily SAT, precipitation, and relative humidity from CN05.1 and daily surface pressure from ERA5 were used to estimate snowfall for 1981–2020. The temperature threshold method proposed by Ding et al. (2014) was adopted here to determine the precipitation type on the basis of the relative humidity and wet-bulb temperature as follows:

$$\mathrm{P_{type}} = \mathrm{snow}, \mathrm{if}\ T_w \le T_{min} \tag{4}$$

where T_w is the daily wet-bulb temperature, which can be deduced as follows:

$$T_w = T_a - \frac{e_{sat}\left(\mathrm{T_a}\right)\left(1 - RH\right)}{0.000643P_s + \frac{\partial \mathrm{e_{sat}}}{\partial \mathrm{T_a}}} \tag{5}$$

where RH is the relative humidity ranging from 0 to 1, T_a is the daily dry-bulb temperature (°C), P_s is the daily air pressure (hPa), and $e_{sat}\left(T_a\right)$ is the saturation vapour pressure (hPa) at T_a calculated by Tetens's empirical formula (Murray 1967):

$$e_{sat}\left(\mathrm{T_a}\right) = 6.1078 \times e^{\left(\frac{17.27T_a}{T_a + 237.3}\right)} \tag{6}$$

where T_{min} is the temperature for equal occurrence probabilities of snow and sleet. It can be expressed as follows:

$$T_{min} = \begin{cases} T_0 - \Delta S \times ln\left[e^{\left(\frac{\Delta T}{\Delta S}\right)} - 2 \times e^{\left(-\frac{\Delta T}{\Delta S}\right)}\right] & \frac{\Delta T}{\Delta S} > ln2 \\ T_0 & \frac{\Delta T}{\Delta S} \leqslant ln2 \end{cases} \tag{7}$$

where ΔT and ΔS represent the temperature difference and temperature scale, respectively. These values are calculated on the basis of their dependences on the RH and given by the following equations:

$$\Delta \mathrm{T} = 0.215 - 0.099 \times \mathrm{RH} + 1.018 \times \mathrm{RH}^2 \tag{8}$$

$$\Delta \mathrm{S} = 2.374 - 1.634 \times \mathrm{RH} \tag{9}$$

The value of T_0 depends on both the RH and elevation and is given by the following equation:

$$T_0 = -5.87 - 0.1042 \times \mathrm{Z} + 0.0885 \times \mathrm{Z}^2 + 16.06 \times \mathrm{RH} - 9.614 \times \mathrm{RH}^2 \tag{10}$$

where Z denotes the elevation (km) of the observation station.

2.1.5 Snow depth

A long time series dataset of daily snow depth in China provided by the National Tibetan Plateau Data Center (Che et al. 2015) was also utilized in this study. The dataset is available at a 0.25°×0.25° spatial resolution covering 1979–2023. More detailed information for this product can be found in the literature (Che et al. 2008; Dai et al. 2015, 2017). This product has been widely used in climatic and hydrological research in China (Wu et al. 2021; Yang et al. 2022). We used data from 1981 to 2020 from this dataset.

The analysis of the impact of BC on surface processes related to the ATC amplitude was based on the observational and reanalysis datasets mentioned above from 1981 to 2020.

2.2 Models and related analysis methods

2.2.1 Simulation

First, to investigate the roles of different external forcings in ATC changes over the TP, eleven CMIP6 (Eyring et al. 2016) models with single-forcing simulations were used. To increase the sample size for a more robust trend analysis, the historical simulations covering 1850–2014 were extended to 2020 following the Shared Socioeconomic Pathway 2-Representative Concentration Pathway 4.5 (SSP2-4.5) emission scenario, an approach that is consistent with methodologies employed in previous relevant studies (e.g., Jiang et al. 2023). The hist-nat, hist-aer, and hist-GHG simulations are forced by natural variability, anthropogenic aerosols or greenhouse gases, respectively. To ensure temporal consistency with the CN05.1 observations, the detection and attribution analysis employed historical simulations from 1961 to 2020. Preindustrial control (piControl) simulations of the eleven models were

used to estimate natural internal climate variability. On the basis of the CMIP6 simulations, the optimal fingerprinting method (Allen and Stott P 2003; Ribes et al. 2013) was used for the detection and attribution of long-term changes in the ATC amplitude. Model selection was made from the pool of models that met two principal criteria: the provision of all necessary forcing outputs for the detection and attribution analysis and a demonstrated reasonable simulation of the observed elevational variations in seasonal warming contrasts over the TP. From this pool, we selected the models detailed in Table S1.

In addition, to demonstrate that BC aerosols intensify high-elevation snow darkening over the TP and subsequently increase surface warming, simulated related variables from three models in the Aerosol Chemistry Model Intercomparison Project (AerChemMIP) endorsed by CMIP6 were also examined. The three models selected for this analysis (GISS-E2-1-G, NorESM2-LM, and UKESM1-0-LL) provided all the required variables and demonstrated a basic ability to reproduce the observed signature of seasonal warming differences with elevation. The impact of BC was assessed using the three AerChemMIP models by contrasting two simulations: (a) the control experiment, which used 1850 concentrations of well-mixed greenhouse gases and emissions of near-term climate forcers (piClim-control); and (b) the perturbation experiment, which used the same forcings but with the BC emissions set to present-day (2014) values (Collins et al. 2017) (piClim-BC). The BC-induced anomalies could be diagnosed by comparing the changes in variables between the two simulations.

Moreover, the surface albedo in the models was expressed as the ratio between surface upward and downward shortwave radiative fluxes because of the lack of albedo variables in the outputs.

2.2.2 Optimal fingerprint detection and attribution

On the basis of total least-square regression, the optimal fingerprint method can be expressed as follows (Allen and Stott P 2003; Ribes et al. 2013):

$$\mathrm{y} = \sum_{\mathrm{i}=1}^{\mathrm{m}} \beta_{\mathrm{i}} \mathrm{X}_{\mathrm{i}} + \varepsilon \tag{11}$$

where y is the observation vector, X_i is the model-simulated response pattern to the ith external forcing, β denotes a vector of regression coefficients or the scaling factors to be estimated, and ε is the internal climate variability. Here, the regularized optimal fingerprinting algorithm was used, which is a specific version that does not rely on empirical orthogonal function (EOF) decomposition (Ribes et al. 2013). The time series was processed as a 5-year nonoverlapping continuous mean with 12 values to filter out the interannual oscillation signal and improve the signal-to-noise ratio. We used two independent estimates of internal climate variability covariances for optimal estimation and residual consistency testing (Zhang et al. 2007). The overall drift of the piControl simulations was removed by subtracting a linear trend over the full period. Moreover, on the basis of Monte Carlo simulations, a residual consistency test was adapted to check whether the noise estimate was consistent with the assumed internal climate variability. Details of the regularized optimal fingerprinting algorithm can be found in the literature (Ribes et al. 2013). Detection and attribution analysis was performed for 1961–2020.

2.3 Statistical significance testing methods

In this study, statistical significance for Pearson correlation and linear regression analyses was assessed using a two-tailed Student's t-test. Student's t-test was also applied to examine the statistical significance of differences between variables with and without BC. Additionally, a residual consistency test based on Monte Carlo simulations was employed within the optimal fingerprinting method for detection and attribution analysis.

3 Results

3.1 Amplitude of the ATC over the TP

The SAT series averaged over the TP was obtained by calculating the means of the grid points above 2000 m from the observations (purple line in Fig. 1a). On the basis of the monthly SAT of the TP, the variability at different frequencies was decomposed via EEMD (Fig. 1a). The data in Fig. 1a clearly show that the modulated annual cycle (MAC) was the dominant component (orange line), explaining 90.8% of the total variance in the monthly mean temperature across the TP from 1961 to 2020. The high-frequency (HF) and low-frequency (LF) components explained 0.6% and 7.6% of the total variance, respectively. Therefore, the annual cycle is the dominant variable at the monthly time scale for the SAT over the TP.

The grid points above 2000 m across the TP were divided into several elevation ranges with 50-m intervals to detect the changes in certain variables with elevation. The mean trends in the summer (red line in Fig. 1b) and winter (blue line in Fig. 1b) temperatures from 1961 to 2020 in the 50-m elevation categories displayed varying extents of warming from 2000 m to above 5000 m, with a noticeable warming difference occurring at elevations of approximately 4000–5300 m. This resulted in a significant decrease in the ATC amplitude above 4000 m, with the most notable weakening occurring mainly at elevations of approximately 4500–5300 m (green line in Fig. 1b). To illustrate the contribution of the SAT in summer and winter to the changes in the ATC amplitude at elevations of 4000–5300 m, where the ATC amplitude decreased significantly ($p<0.05$), their relationships are quantified and presented in Fig. 1c. The ATC amplitude trend over the TP from 1961 to 2020 did not significantly correlate with the summer temperature trend (Fig. 1c). However, the correlation between the winter temperature trend and amplitude trend was significant (Fig. 1c), with a correlation coefficient of −0.777 ($p<0.01$). Consequently, the decreasing ATC amplitude over the high-elevation TP was most closely related to the change in the winter temperature.

3.2 Attribution analysis

The multimodel ensemble mean (MME) of the eleven CMIP6 models reasonably captured the more prominent weakening in the ATC amplitude in the higher elevation regions above approximately 4000 m (Fig. 2a), which was consistent with the observations (Fig. 1b). According to the two-signal analyses with passed residual consistency tests, we found that the change in the ATC amplitude at elevations between 4000 and 5300 m could be attributed mainly to anthropogenic activities, with anthropogenic aerosol forcing playing a dominant

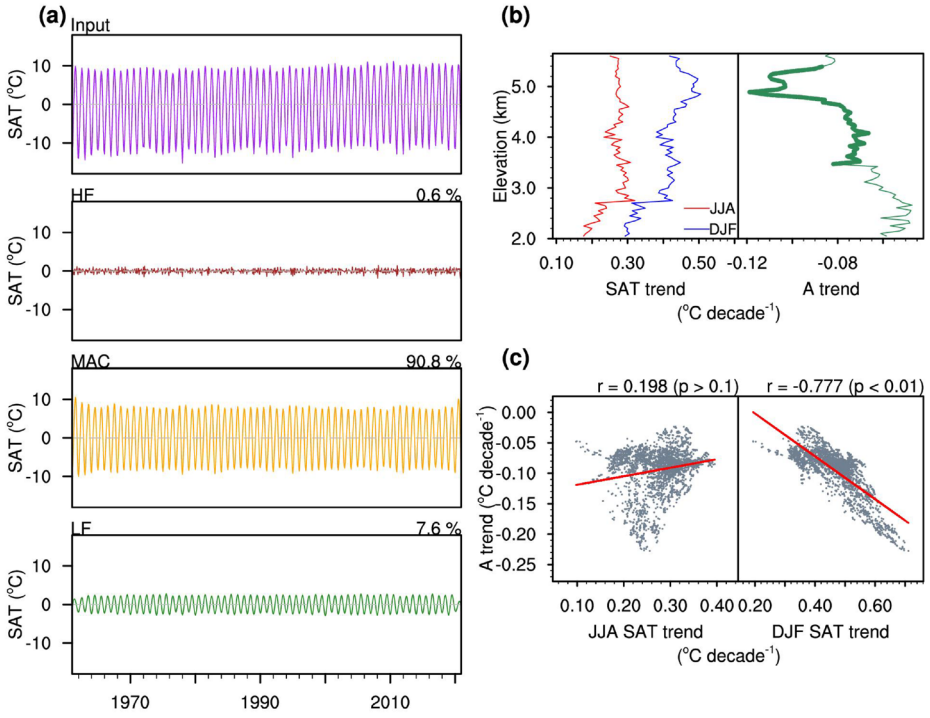

Fig. 1 (**a**) Raw monthly surface air temperature (SAT, in purple) and its variability 3 at different frequencies decomposed by the EEMD filter over the TP at elevations above 2000 m for 1961–2020. The three components in the schematic diagram include the intra-annual high-frequency variability (HF, in brown), modulated annual cycle (MAC, in orange), and interannual to decadal low-frequency variability (LF, in green). The explained variance for each component is shown in the upper-right corner of each graph. (**b**) Mean trends in the SAT and ATC amplitude (A) in the observations for the 50-m elevation zones. A thicker line indicates statistical significance above the 95% confidence level. (**c**) Relationships between the trends in the ATC amplitude and the summer temperature (JJA SAT) and winter temperature (DJF SAT) trends at elevations of 4000–5300 m. The correlation coefficient (R) and the P value of the linear regression (red solid line) are also shown

role (Fig. 2b). At elevations of 4000–5300 m, the scaling factors were significantly greater than zero and were consistent with 1 for simulations under both anthropogenic forcing and aerosol forcing in the two-signal analyses for the ANT-NAT and AER-GHG forcings (Fig. 2b). These findings indicate that the effects of ANT and AER forcing were detectable and separable from those of NAT and GHG forcing. However, the residual consistency test failed in the case of elevations from 2000 to 4000 m (Figure S2). Hence, human activities, predominantly through anthropogenic aerosol forcing, accounted for most of the ATC amplitude change at elevations of 4000–5300 m over the TP.

3.3 BC impacts on the ATC amplitude and the associated mechanisms

As one of the key drivers of cryospheric changes, BC increased significantly over most of the TP during the winter of 1981–2020, as evidenced by its surface mass concentration (BCSMASS; Fig. 3a). BC may increase winter warming through reducing the snow

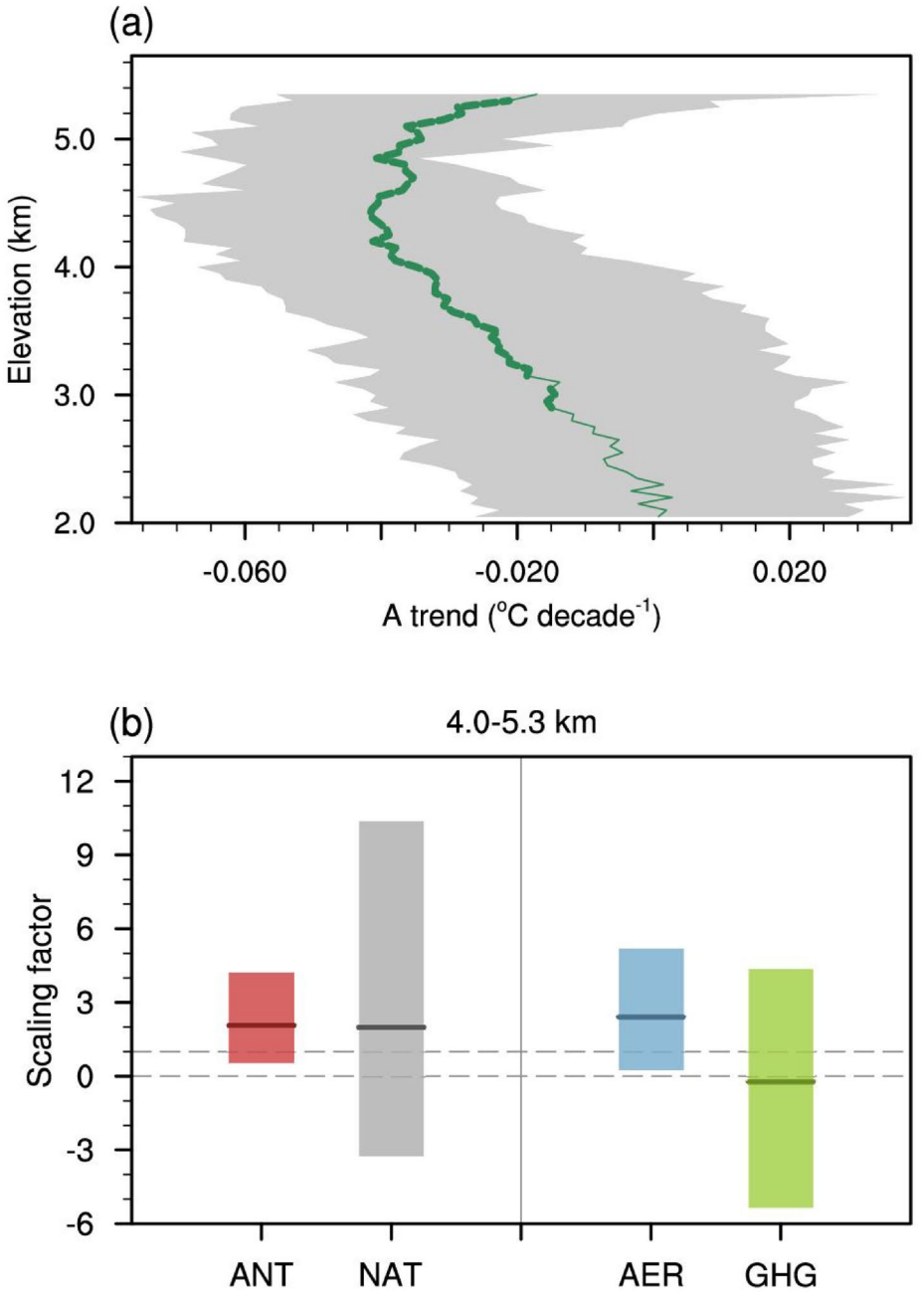

Fig. 2 (**a**) Mean trend in the ATC amplitude (A) in the multimodel ensemble 17 mean under ALL forcing for the 50-m elevation zones. A thicker line indicates statistical significance above the 95% confidence level. The grey shading represents the 25th to 75th percentile range of trends across the ensemble members. (**b**) Optimal fingerprint detection and attribution analysis of the changes in the ATC amplitude at elevations between 4000 and 5300 m across the TP from 1961–2020. The lines denote the scaling factors of the two-signal analysis for ANT and NAT and for the AER and GHG forcings. The error bars denote the corresponding 90% confidence intervals. The residual consistency test is passed in both cases

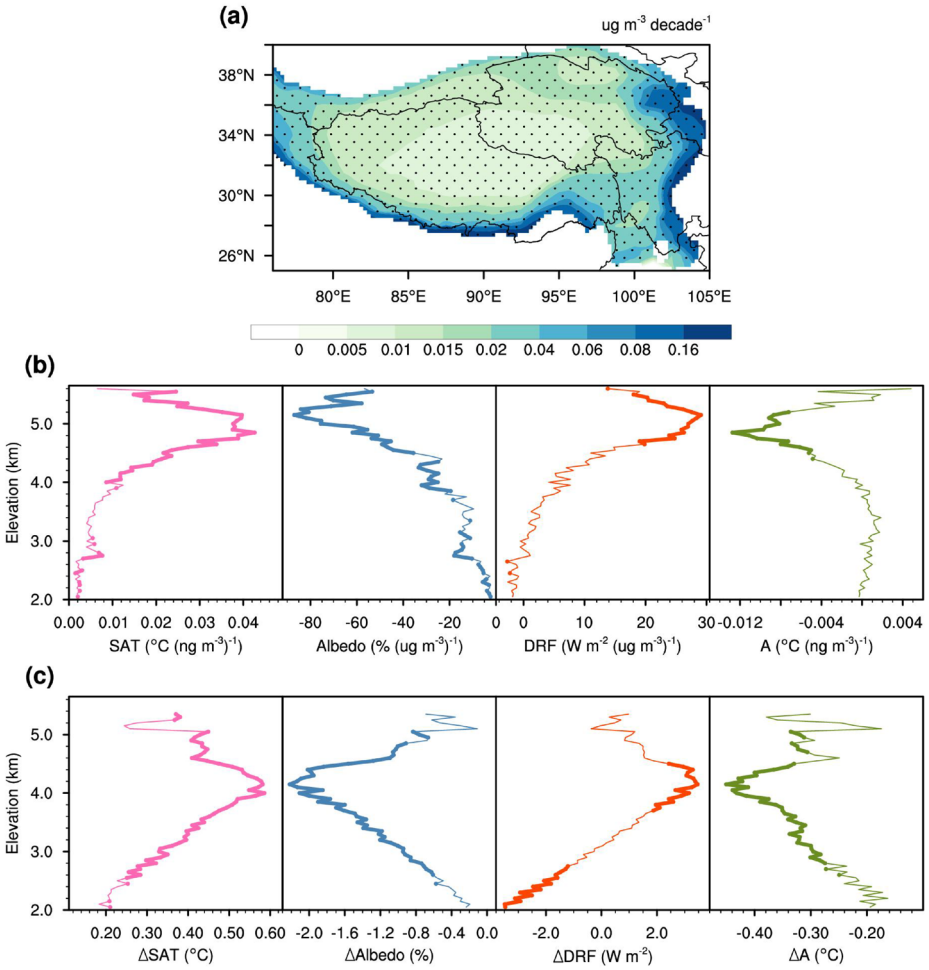

Fig. 3 (**a**) Linear trend in the BCSMASS from the MERRA-2 reanalysis data 29 for the region of the TP above 2000 m in DJF from 1981–2020. The black dots represent significant trends ($p < 0.05$). (**b**) Mean linear regression coefficient of the BCSMASS against the winter (DJF) SAT, albedo, direct radiative forcing (DRF), and ATC amplitude (A) for the 50-m elevation zones. (**c**) Mean elevation dependence of BC-induced anomalies in winter (DJF) SAT, albedo, DRF, and ATC amplitude in the multimodel ensemble mean (Δ: variables with BC minus variables without BC). A thicker line indicates statistical significance above the 90% confidence level

albedo and increasing shortwave radiative absorption, leading to a weakened ATC amplitude. To assess the influence of BC on the ATC amplitude, the linear regression coefficients of BCSMASS regressed on SAT, albedo, direct radiative forcing, and ATC amplitude within each elevation bin in winter were determined (Fig. 3b). Moreover, to further examine these observed relationships, the mean elevational distribution of the BC-induced anomalies in the aforementioned variables was evaluated using the piClim-control and piClim-BC experiments (Fig. 3c). In the TP region below 5000 m, the regression coefficient of the SAT onto BCSMASS increased with elevation, reaching its maximum near 5000 m (Fig. 3b; in hot

pink), which indicates that the sensitivity of the SAT to BC aerosols was most pronounced at higher elevations, particularly at approximately 5000 m. The model simulations (piClim-BC vs. piClim-control) also showed an increasing sensitivity with elevation, but the peak occurred at a lower elevation of approximately 4000 m (Fig. 3c; in hot pink). Thus, both the observations and the models suggest a stronger BC impact on the SAT in the high-elevation zone, although the exact elevation of the maximum effect differs: the observations point to approximately 5000 m, whereas the models place it at approximately 4000 m. This discrepancy may stem from model biases in simulating the snow depth distribution, as discussed later.

Similarly, both observations and models indicated that BC-induced changes in albedo, direct radiative forcing, and ATC amplitude increased with elevation and reached their maximum values in the high-elevation zone (Fig. 3b, c, steel blue, orange-red, and olive drab, respectively). In the observations, these maxima occurred in the uppermost part of the 4000–5300 m range, particularly near 5000 m (Fig. 3b). The models again exhibited a similar elevational dependence, although the maxima were shifted to approximately 4000 m (Fig. 3c). Consequently, both observations and models revealed that the BC-induced surface albedo reduction increased with elevation, with the strongest reduction occurring near 5000 m in the observations and approximately 4000 m in the models (Fig. 3b, c; in steel blue). The positive direct radiative forcing from snow darkening also increased with elevation in both datasets, peaking at approximately 5000 m in the observations and at 4000 m in the models (Fig. 3b, c; in orange-red). This elevation-dependent warming led to a corresponding decrease in the ATC amplitude at higher elevations in both the observations and the models, with the most pronounced decrease observed near 5000 m in the observations and approximately 4000 m in the models (Fig. 3b, c; in olive drab). Overall, while the exact a elevation of the maximum effect differed, both observational and model evidence consistently revealed to a stronger BC impact on these variables in the high-elevation zone.

This spatial pattern is indicative of an underlying mechanism tied to the snowpack state. That mechanism is most active where persistent, aged snow accumulates. The snow line in a given year is usually defined by the lower limit of the annual snowpack distribution height in the warmest month of that year. Aged snow is generally distributed in regions above the multiyear average elevation of the snow line. The elevational distributions of BCSMASS and snowfall in winter, as well as the snow depth in July, are shown in Fig. 4. Over the TP from 1981 to 2020, although BCSMASS increased more below 3800 m (Fig. 4a), the albedo darkening effect caused by BC was suppressed because of the absence of aged snow (Fig. 4b). Hence, the albedo abnormality triggered by BC did not dramatically decrease below 3800 m (Fig. 3b; in steel blue). On average, the aged snow was distributed mainly at elevations above 4000 m on the TP, with the maximum snow thickness centred at approximately 4800–5300 m (Fig. 4b). The most marked decrease in albedo (Fig. 3b; in steel blue) occurred precisely where aged snow was thicker (Fig. 4b) and where snowfall did not increase significantly (Fig. 4c). These findings indicated that the snow-darkening effect triggered by BC depended not only on the BC mass concentration but also on the aged snow thickness and snowpack microphysics associated with snow grain size and metamorphism with ageing on the TP.

The discrepancy between the observed and modelled elevational peaks can be explained by the underestimation of snow depth by the MME at higher elevations (Fig. 3c). As shown in Fig. S3, the MME simulated greater snow thickness mainly between 3800 and 4400 m,

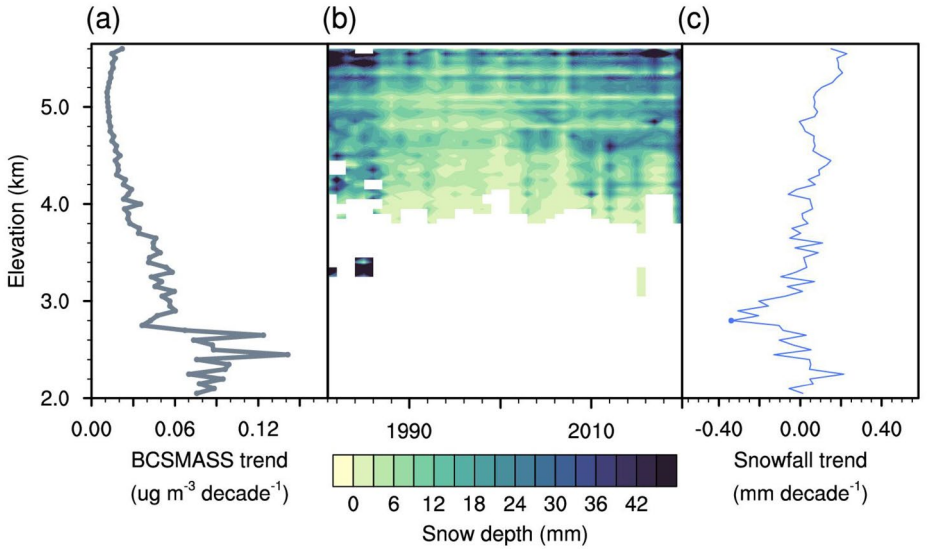

Fig. 4 Mean elevation dependence of the linear trend for (**a**) the BCSMASS 41 from the MERRA-2 reanalysis data and (**c**) snowfall calculated in our study over the TP in DJF from 1981–2020. A thicker line indicates statistical significance above the 90% confidence level. (**b**) Elevation-dependent variation in snow depth over the TP from 1981–2020 in July from the observations

which was lower than the observed zone of maximum aged snow (above 4800 m). Similarly, the BC-induced anomalies in SAT, albedo, radiative forcing, and ATC amplitude all peaked near the modelled maximum snow-depth.

4 Conclusion and discussion

A negative trend in the ATC amplitude was observed to intensify on the TP at elevations above approximately 4000 m. Our analysis revealed that this intensification was driven primarily by stronger warming in winter than in summer. Anthropogenic aerosols played a dominant role in the change in the ATC amplitude at elevations above 4000 m. The albedo darkening triggered by increased BC aerosols in winter accounted for the decreased ATC amplitude at higher elevations of the TP. The most robust sensitivity of the surface albedo to the change in BC aerosols occurred at higher elevations, where there are typically greater aged snow depths and limited fresh snowfall. This pattern points to the involvement of the grain-size feedback, which is augmented by the temporal accumulation of BC. BC deposition decreases the surface albedo in the presence of snow. This direct surface darkening effectively accelerates snow grain growth, which then speeds up snow ageing and further reduces the snow albedo. This phenomenon is known as the grain-size feedback (Skiles et al. 2018). Furthermore, in perennial snowpacks, BC can accumulate over multiple seasons, leading to higher effective concentrations at the surface (Doherty et al. 2013; Xu et al. 2009), whereas seasonal snowfall resets the BC burden annually (Qian et al. 2015). Therefore, the efficiency and magnitude of BC-induced snow albedo decay are greater for aged snowpack because of this combination of physical amplification (via larger grain sizes) and higher

cumulative BC loading (Doherty et al. 2013; He et al. 2018; Niu et al. 2017; Usha et al. 2021). This coarse-grained snow with greater aged snow depths and limited fresh snowfall enhances the surface darkening effect triggered by BC more efficiently. Collectively, snow optical properties are synthetically dominated by snow grain properties (that is, size, shape and metamorphism with ageing) and the concentrations of light-absorbing particles (Dang et al. 2016; Sarangi et al. 2020; Wang et al. 2020; Warren 2019). Relative to surface mass concentration, the factors associated with the snow grain properties and multiseasonal BC accumulation, such as the amount of aged snow are essential for enhancing the efficiency of BC-induced snow albedo darkening over the TP. In the region where surface albedo is sensitive to changes in BC, BC-triggered albedo decay may significantly reduce the ATC amplitude by increasing surface absorbed shortwave radiation and accelerating warming in the winter.

Our results align with and extend those of previous studies documenting a widespread reduction in the ATC amplitude over extratropical land areas (Duan et al. 2019; Stine et al. 2009; Wang and Dillon 2014), including the TP (Duan et al. 2017), for which the underlying mechanisms—especially the relative roles of aerosols over the high-elevation TP—have remained unclear. This study clarifies the specific impact of BC aerosols on the reduced ATC amplitude over the high-elevation TP. By establishing a mechanistic basis for BC-driven winter warming, our study provides a key link to understanding how trends in BC emissions could directly influence high-elevation snowmelt, thereby potentially affecting regional hydrology and water resources. These results not only highlight the climate co-benefit of aerosol mitigation for cryospheric conservation but also provide a critical scientific basis for the adaptive management of alpine ecosystems and future climate impact assessments.

Several caveats should be considered when our results are interpreted. First, the analysis relies on CMIP6 simulations, which exhibit known biases in representing the TP climate, particularly in simulating snow depth and aerosol–snow interactions. The lower elevation of the maximum snow depth in the models likely explains the slight downward shift in the simulated sensitive zone of albedo darkening relative to the observations. Second, to elucidate the physical process, this study utilized standardized "idealized perturbation" experiments (piClim-control vs. piClim-BC) from AerChemMIP. These publicly available simulations are specifically designed to isolate the climate response to perturbations in BC emissions and provide key evidence supporting the proposed snow–albedo feedback mechanism. To further quantify and refine this understanding, future work could benefit from designing and conducting additional sensitivity experiments with regionally tailored BC emission scenarios, particularly using high-resolution regional climate models that incorporate more sophisticated snow–aerosol–microphysics coupling. Such targeted simulations would help to constrain the magnitude of the feedback and better represent the complex interactions over the heterogeneous terrain of the Tibetan Plateau.

Supplementary Information The online version contains supplementary material available at https://doi.org/10.1007/s10584-026-04192-7.

Acknowledgements The gridded observational dataset was provided by the Climate Change Research Center, Chinese Academy of Sciences (https://ccrc.iap.ac.cn/resource). The GLASS data were supported by National Earth System Science Data Center, National Science & Technology Infrastructure of China (http://www.geodata.cn). The long time series dataset of daily snow depth in China was provided by National Tibetan Plateau Data Center (http://data.tpdc.ac.cn).

Author contributions L. Zhu conceived the research, performed the analysis and drafted the manuscript. W. Hua provided comments. G. Huang and X. Lai contributed to scientific interpretations.

Funding This work was supported by the National Natural Science Foundation of China (42575187), Sichuan Science and Technology Program (2025NSFSC2005), the Second Tibetan Plateau Scientific Expedition and Research program (2019QZKK010203).

Data availability The gridded observational datasets (CN05.1) are available from https://ccrc.iap.ac.cn/resource. The MERRA-2 reanalysis data used in this study can be downloaded from https://disc.gsfc.nasa.gov/. The GLASS data are available online at http://www.geodata.cn. ERA5 data are available online at https://www.ecmwf.int/. The long time series dataset of daily snow depth in China is available from http://data.tpdc.ac.cn. The model outputs of CMIP6 community are available at https://esgf-node.llnl.gov/projects/cmip6/.

Declarations

Competing interests The authors declare no competing interests.

References

Allen MR, Stott PA (2003) Estimating signal amplitudes in optimal fingerprinting, Part I: theory. Clim Dyn 21(5–6):477–491. https://doi.org/10.1007/s00382-003-0313-9

An Y, Meng X, Zhao L, Li Z, Wang S, Shang L, Chen H, Lyu S, Li G, Ma Y (2020) Performance of GLASS and MODIS satellite albedo products in diagnosing albedo variations during different time scales and special weather conditions in the Tibetan Plateau. Remote Sens 12(15):2456. https://doi.org/10.3390/rs12152456

Antón M, Gil JE, Fernández-Gálvez J, Lyamani H, Valenzuela A, Foyo-Moreno I, Olmo FJ, Alados-Arboledas L (2011) Evaluation of the aerosol forcing efficiency in the UV erythemal range at Granada, Spain. J. Geophys. Res 116(D20):D20214. https://doi.org/10.1029/2011JD016112

Buchard V, da Silva AM, Colarco PR, Darmenov A, Randles CA, Govindaraju R, Torres O, Campbell J, Spurr R (2015) Using the OMI aerosol index and absorption aerosol optical depth to evaluate the NASA MERRA aerosol reanalysis. Atmos Chem Phys 15(10):5743–5760. https://doi.org/10.5194/acp-15-5743-2015

Buizert C, Keisling BA, Box JE, He F, Carlson AE, Sinclair G, DeConto RM (2018) Greenland-wide seasonal temperatures during the last deglaciation. Geophys Res Lett 45(4):1905–1914. https://doi.org/10.1002/2017GL075601

Bujan J, Roeder KA, Yanoviak SP, Kaspari M (2020) Seasonal plasticity of thermal tolerance in ants. Ecology 101(6):e03051. https://doi.org/10.1002/ecy.3051

Che T, Dai L, Li X (2015) Long-term series of daily snow depth dataset in China (1979-2021). A Big Earth Data Platform for Three Poles [data set]. https://doi.org/10.11888/Geogra.tpdc.270194

Che T, Li X, Jin R, Armstrong R, Zhang TJ (2008) Snow depth derived from passive microwave remote-sensing data in China. Ann Glaciol 49:145–154. https://doi.org/10.3189/172756408787814690

Chen A, Hu C, Bian L, Liu Y (2015) An assessment on the accuracy of the GLASS albedo products over the Tibetan Plateau (in Chinese). Acta Meteorol Sin 73(6):1114–1120. https://doi.org/10.11676/qxxb2015.074

Chen Y, Ji D, Moore JC, Hu J, He Y (2022) Observational constraint on the contribution of surface albedo feedback to the amplified Tibetan Plateau surface warming. JGR Atmospheres 127(13):e2021JD036085. https://doi.org/10.1029/2021JD036085

Cheng C, He N, Li M, Xu L, Cai W, Li X, Zhao W, Li C, Sun O J (2023) Plant species richness on the Tibetan Plateau: patterns and determinants. Ecography 2023(1):e06265. https://doi.org/10.1111/ecog.06265

Choi G, Robinson DA, Kang S (2010) Changing Northern Hemisphere snow seasons. J Educ Chang Clim 23(19):5305–5310. https://doi.org/10.1175/2010JCLI3644.1

Collins WJ, Lamarque J-F, Schulz M, Boucher O, Eyring V, Hegglin MI, Maycock A, Myhre G, Prather M, Shindell D, Smith SJ (2017) AerChemMIP: quantifying the effects of chemistry and aerosols in CMIP6. Geosci Model Dev 10(2):585–607. https://doi.org/10.5194/gmd-10-585-2017

Dai LY, Che T, Ding YJ (2015) Inter-calibrating SMMR, SSM/I and SSMI/S data to improve the consistency of snow-depth products in China. Remote Sens 7(6):7212–7230. https://doi.org/10.3390/rs70607212

Dai LY, Che T, Ding YJ, Hao XH (2017) Evaluation of snow cover and snow depth on the Qinghai–Tibetan Plateau derived from passive microwave remote sensing. Cryosphere 11(4):1933–1948. https://doi.org/10.5194/tc-11-1933-2017

Dang C, Fu Q, Warren SG (2016) Effect of snow grain shape on snow albedo. J Atmos Sci 73(9):3573–3583. https://doi.org/10.1175/JAS-D-15-0276.1

Di Mauro B (2020) A darker cryosphere in a warming world. Nat. Clim. Chang. 10(11):979–980. https://doi.org/10.1038/s41558-020-00911-9

Ding B, Yang K, Qin J, Wang L, Chen Y, He X (2014) The dependence of precipitation types on surface elevation and meteorological conditions and its parameterization. J Hydrol 513:154–163. https://doi.org/10.1016/j.jhydrol.2014.03.038

Doherty SJ, Grenfell TC, Forsström S, Hegg DL, Brandt RE, Warren SG (2013) Observed vertical redistribution of black carbon and other insoluble light-absorbing particles in melting snow. JGR Atmospheres 118(11):5553–5569. https://doi.org/10.1002/jgrd.50235

Duan J, Esper J, Büntgen U, Li L, Xoplaki E, Zhang H, Wang L, Fang Y, Luterbacher J (2017) Weakening of annual temperature cycle over the Tibetan Plateau since the 1870s. Nat Commun 8(1):14008. https://doi.org/10.1038/ncomms14008

Duan J, Ma Z, Wu P, Xoplaki E, Hegerl G, Li L, Schurer A, Guan D, Chen L, Duan Y, Luterbacher J (2019) Detection of human influences on temperature seasonality from the nineteenth century. Nat Sustain 2(6):484–490. https://doi.org/10.1038/s41893-019-0276-4

Eyring V, Bony S, Meehl GA, Senior CA, Stevens B, Stouffer RJ, Taylor KE (2016) Overview of the coupled model intercomparison project phase 6 (CMIP6) experimental design and organization. Geosci Model Dev 9(5):1937–1958. https://doi.org/10.5194/gmd-9-1937-2016

Feng X, Mao R, Gong DY, Zhao C, Wu C, Zhao C, Wu G, Lin Z, Liu X, Wang K, Sun Y (2020) Increased dust aerosols in the high troposphere over the Tibetan Plateau from 1990s to 2000s. JGR Atmospheres 125(13):e2020JD032807. https://doi.org/10.1029/2020JD032807

Fisher DA, Lacelle D, Pollard W (2020) A model of unfrozen water content and its transport in icy permafrost soils: effects on ground ice content and permafrost stability. Permafrost & Periglacial 31(1):184–199. https://doi.org/10.1002/ppp.2031

Fisher DA, Lacelle D, Pollard W, Davila A, McKay CP (2016) Ground surface temperature and humidity, ground temperature cycles and the ice table depths in University Valley, McMurdo Dry valleys of Antarctica. JGR Earth Surf 121(11):2069–2084. https://doi.org/10.1002/2016JF004054

Gelaro R, McCarty W, Suárez M, Todling R, Molod A, Takacs L, Randles CA, Darmenov A, Bosilovich M G, Reichle R, Wargan K, Coy L, Cullather R, Draper C, Akella S, Buchard V, Conaty A, da Silva AM, Gu W, Kim GK, Koster R, Lucchesi R, Merkova D, Nielsen JE, Partyka G, Pawson S, Putman W, Rienecker M, Schubert SD, Sienkiewicz M, Zhao B, Suárez MJ (2017) The Modern-Era Retrospective analysis for Research and Applications, version 2 (MERRA-2). J Clim 30(14):5419–5454. https://doi.org/10.1175/JCLI-D-16-0758.1

Hamlet AF, Mote PW, Clark MP, Lettenmaier DP (2005) Effects of temperature and precipitation variability on snowpack trends in the Western United States. J Educ Chang Clim 18(21):4545–4561. https://doi.org/10.1175/JCLI3538.1

He C, Flanner MG, Chen F, Barlage M, Liou KN, Kang S, Ming J, Qian Y (2018) Black carbon-induced snow albedo reduction over the Tibetan Plateau: uncertainties from snow grain shape and aerosol–snow mixing state based on an updated SNICAR model. Atmos Chem Phys 18(15):11507–11527. https://doi.org/10.5194/acp-18-11507-2018

He T, Liang S, Song D (2014) Analysis of global land surface albedo climatology and spatial-temporal variation during 1981–2010 from multiple satellite products. JGR Atmospheres 119(17):10281–10298. https://doi.org/10.1002/2014JD021667

He T, Liang S, Yu Y, Wang D, Gao F, Liu Q (2013) Greenland surface albedo changes in July 1981–2012 from satellite observations. Environ Res Lett 8(4):004043. https://doi.org/10.1088/1748-9326/8/4/044043

Hori M, Sugiura K, Kobayashi K, Aoki T, Tanikawa T, Kuchiki K, Niwano M, Enomoto H (2017) A 38-year (1978–2015) Northern Hemisphere daily snow cover extent product derived using consistent objective criteria from satellite-borne optical sensors. Remote Sens Environ 191:402–418. https://doi.org/10.1016/j.rse.2017.01.023

Jennings KS, Winchell TS, Livneh B, Molotch N (2018) Spatial variation of the rain–snow temperature threshold across the Northern Hemisphere. Nat Commun 9(1):1148. https://doi.org/10.1038/s41467-018-03629-7

Jiang J, Zhou T, Qian Y, Li C, Song F, Li H, Chen X, Zhang W, Chen Z (2023) Precipitation regime changes in high mountain Asia driven by cleaner air. Nature 623(7987):544–549. https://doi.org/10.1038/s41586-023-06619-y

Jiang Y, Chen F, Gao Y, He C, Barlage M, Huang W (2020) Assessment of uncertainty sources in snow cover simulation in the Tibetan plateau. JGR Atmospheres 125(18):e2020JD032674. https://doi.org/10.1029/2020JD032674

Kang S, Zhang Q, Qian Y, Ji Z, Li C, Cong Z, Zhang Y, Guo J, Du W, Huang J, You Q, Panday AK, Rupakheti M, Chen D, Gustafsson Ö, Thiemens MH, Qin D (2019) Linking atmospheric pollution to cryospheric change in the third Pole region: current progress and future prospects. Natl Sci Rev 6(4):796–809. https://doi.org/10.1093/nsr/nwz031

Kang S, Zhang Y, Qian Y, Wang H (2020) A review of black carbon in snow and ice and its impact on the cryosphere. Earth-Sci Rev 210:103346. https://doi.org/10.1016/j.earscirev.2020.103346

Kim Y, Kimball JS, Zhang K, McDonald KC (2012) Satellite detection of increasing Northern Hemisphere non-frozen seasons from 1979 to 2008: implications for regional vegetation growth. Remote Sens Environ 121:472–487. https://doi.org/10.1016/j.rse.2012.02.014

Li C, Bosch C, Kang S, Andersson A, Chen P, Zhang Q, Cong Z, Chen B, Qin D, Gustafsson Ö (2016) Sources of black carbon to the Himalayan–Tibetan Plateau glaciers. Nat Commun 7(1):12574. https://doi.org/10.1038/ncomms12574

Li Y, Huang Y, Bergelson J, Nordborg M, Borevitz JO (2010) Association mapping of local climate-sensitive quantitative trait loci in Arabidopsis thaliana. Proc Natl Acad Sci USA 107(49):21199–21204. https://doi.org/10.1073/pnas.1007431107

Liang S, Cheng J, Jia K, Jiang B, Liu Q, Xiao Z, Yao Y, Yuan W, Zhang X, Zhao X, Zhou J (2021) The global land surface satellite (GLASS) product suite. Bull am Meteorolog Soc 102(2):E323–E337. https://doi.org/10.1175/BAMS-D-18-0341.1

Liang S, Zhao X, Liu S, Yuan W, Cheng X, Xiao Z, Zhang X, Liu Q, Cheng J, Tang H, Qu Y, Bo Y, Qu Y, Ren H, Yu K, Townshend J (2013) A long-term Global Land Surface Satellite (GLASS) data-set for environmental studies. Int J Digit Earth 6(sup1):5–33. https://doi.org/10.1080/17538947.2013.805262

Liu C, Yin Z, He Y, Wang L (2022) Climatology of dust aerosols over the jianghan plain revealed with spaceborne instruments and MERRA-2 reanalysis data during 2006–2021. Remote Sens 14(17):4414. https://doi.org/10.3390/rs14174414

Liu L, Guo J, Gong H, Li Z, Chen W, Wu R, Wang L, Xu H, Li J, Chen D, Zhai P (2019) Contrasting influence of Gobi and Taklimakan deserts on the dust aerosols in Western North America. Geophys Res Lett 46(15):9064–9071. https://doi.org/10.1029/2019GL083508

Liu Q, Wang L, Qu Y, Liu N, Liu S, Tang H, Liang S (2013) Preliminary Evaluation of the long-term GLASS albedo product. Int J Digit Earth 6(sup1):69–95. https://doi.org/10.1080/17538947.2013.804601

Ma N, Szilagyi J, Zhang Y, Liu W (2019) Complementary-relationship-based modeling of terrestrial evapotranspiration across China during 1982–2012: validations and spatiotemporal analyses. JGR Atmospheres 124(8):4326–4351. https://doi.org/10.1029/2018JD029850

Mao KS, Wang Y, Liu JQ (2021) Evolutionary origin of species diversity on the Qinghai–Tibet Plateau. J Sytematics Evol 59(6):1142–1158. https://doi.org/10.1111/jse.12809

McKenzie JM, Voss CI (2013) Fusão do permafrost num sistema de fluxo de água subterrâneo encaixado. Hydrogeol J 21(1):299–316. https://doi.org/10.1007/s10040-012-0942-3

Miao X, Guo W, Li W, Cao Y, Ge J, Qiu B (2024) Instant response of Tibetan Plateau surface albedo to snow coverage and depth in snow season. Geophys Res Lett 51(3):e2023GL108010. https://doi.org/10.1029/2023GL108010

Murray FW (1967) On the computation of saturation vapor pressure. J Appl Meteor 6(1):203–204. https://doi.org/10.1175/1520-0450(1967)006%3C0203:OTCOSV%3E2.0.CO;2

Niu H, Kang S, Shi X, Paudyal R, He Y, Li G, Wang S, Pu T, Shi X (2017) In-situ measurements of light-absorbing impurities in snow of glacier on Mt. Yulong and implications for radiative forcing estimates. Sci Total Environ 581-582:848–856. https://doi.org/10.1016/j.scitotenv.2017.01.032

Niu X, Tang J, Chen D, Wang S, Ou T, Fu C (2021) The performance of CORDEX-EA-II simulations in simulating seasonal temperature and elevation-dependent warming over the Tibetan Plateau. Clim Dynam 57(3–4):1135–1153. https://doi.org/10.1007/s00382-021-05760-6

Qian C, Fu C, Wu Z (2011) Changes in the amplitude of the temperature annual cycle in China and their implication for climate change research. J Educ Chang Clim 24(20):5292–5302. https://doi.org/10.1175/JCLI-D-11-00006.1

Qian C, Zhang X (2015) Human influences on changes in the temperature seasonality in mid- to high-latitude land areas. J Educ Chang Clim 28(15):5908–5921. https://doi.org/10.1175/JCLI-D-14-00821.1

Qian Y, Yasunari TJ, Doherty SJ, Flanner MG, Lau WKM, Ming J, Wang H, Wang M, Warren SG, Zhang R (2015) Light-absorbing particles in snow and ice: measurement and modeling of climatic and hydrological impact. Adv Atmos Sci 32(1):64–91. https://doi.org/10.1007/s00376-014-0010-0

Qiu J (2008) China: the third pole. Nature 454(7203):393–396. https://doi.org/10.1038/454393a

Ribes A, Planton S, Terray L (2013) Application of regularised optimal fingerprinting to attribution. Part I: method, properties and idealised analysis. Clim Dynam 41(11–12):2817–2836. https://doi.org/10.1007/s00382-013-1735-7

Richardson AD, Hufkens K, Milliman T, Aubrecht DM, Furze ME, Seyednasrollah B, Krassovski MB, Latimer JM, Robert Nettles W, Heiderman RR, Warren JM, Hanson PJ (2018) Ecosystem warming extends vegetation activity but heightens vulnerability to cold temperatures. Nature 560(7718):368–371. https://doi.org/10.1038/s41586-018-0399-1

Román MO, Schaaf CB, Lewis P, Gao F, Anderson GP, Privette JL, Strahler AH, Woodcock CE, Barnsley M (2010) Assessing the coupling between surface albedo derived from MODIS and the fraction of diffuse skylight over spatially-characterized landscapes. Remote Sens Environ 114(4):738–760. https://doi.org/10.1016/j.rse.2009.11.014

Sarangi C, Qian Y, Rittger K, Ruby Leung L, Chand D, Bormann KJ, Painter TH (2020) Dust dominates high-altitude snow darkening and melt over high-mountain Asia. Nat. Clim. Chang. 10(11):1045–1051. https://doi.org/10.1038/s41558-020-00909-3

Shepherd A, Fricker HA, Farrell SL (2018) Trends and connections across the Antarctic cryosphere. Nature 558(7709):223–232. https://doi.org/10.1038/s41586-018-0171-6

Shi Y, Wang G, Gao X (2018) Role of resolution in regional climate change projections over China. Clim Dynam 51(5–6):2375–2396. https://doi.org/10.1007/s00382-017-4018-x

Shrestha N, Su X, Xu X, Wang Z (2018) The drivers of high rhododendron diversity in south-west China: does seasonality matter? J Retailing Biogeogr 45(2):438–447. https://doi.org/10.1111/jbi.13136

Skiles SM, Flanner M, Cook JM, Dumont M, Painter TH (2018) Radiative forcing by light-absorbing particles in snow. Nat Clim Change 8(11):964–971. https://doi.org/10.1038/s41558-018-0296-5

Steinbauer MJ, Grytnes JA, Jurasinski G, Kulonen A, Lenoir J, Pauli H, Rixen C, Winkler M, Bardy-Durchhalter M, Barni E, Bjorkman AD, Breiner FT, Burg S, Czortek P, Dawes MA, Delimat A, Dullinger S, Erschbamer B, Felde VA, Fernández-Arberas O, Fossheim KF, Gómez-García D, Georges D, Grindrud ET, Haider S, Haugum SV, Henriksen H, Herreros MJ, Jaroszewicz B, Jaroszynska F, Kanka R, Kapfer J, Klanderud K, Kühn I, Lamprecht A, Matteodo M, Morra di Cella U, Normand S, Odland A, Olsen SL et al (2018) Accelerated increase in plant species richness on mountain summits is linked to warming. Nature 556(7700):231–234. https://doi.org/10.1038/s41586-018-0005-6

Stine A, Huybers P, Fung I (2009) Changes in the phase of the annual cycle of surface temperature. Nature 457(7228):435–440. https://doi.org/10.1038/nature07675

Usha KH, Nair VS, Babu SS (2021) Effect of aerosol-induced snow darkening on the direct radiative effect of aerosols over the Himalayan region. Environ Res Lett 16(6):064004. https://doi.org/10.1088/1748-9326/abf190

Vicente Liz A, Santos V, Ribeiro T, Guimaraes M, Verrastro L (2019) Are lizards sensitive to anomalous seasonal temperatures? long-term thermobiological variability in a subtropical species. PLoS One 14(12):e0226399. https://doi.org/10.1371/journal.pone.0226399

Wan X, Kang S, Li Q, Rupakheti D, Zhang Q, Guo J, Chen P, Tripathee L, Rupakheti M, Panday AK, Wang W, Kawamura K, Gao S, Wu G, Cong Z (2017) Organic molecular tracers in the atmospheric aerosols from Lumbini, Nepal, in the northern Indo-Gangetic plain: influence of biomass burning. Atmos Chem Phys 17(14):8867–8885. https://doi.org/10.5194/acp-17-8867-2017

Wang G, Dillon M (2014) Recent geographic convergence in diurnal and annual temperature cycling flattens global thermal profiles. Nat Clim Change 4(11):988–992. https://doi.org/10.1038/nclimate2378

Wang X, Shi T, Zhang X, Chen Y (2020) An Overview of snow albedo sensitivity to black carbon contamination and snow grain properties based on experimental datasets across the Northern Hemisphere. Curr Pollut Rep 6(4):368–379. https://doi.org/10.1007/s40726-020-00157-1

Warren SG (2019) Optical properties of ice and snow. Phil Trans R Soc A 377(2146):20180161. https://doi.org/10.1098/rsta.2018.0161

Weyhenmeyer GA, Obertegger U, Rudebeck H, Jakobsson E, Jansen J, Zdorovennova G, Bansal S, Block BD, Carey CC, Doubek JP, Dugan H, Erina O, Fedorova I, Fischer JM, Grinberga L, Grossart H-P, Kangur K, Knoll LB, Laas A, Lepori F, Meier J, Palshin N, Peternell M, Pulkkanen M, Rusak JA, Sharma S, Wain D, Zdorovennov R (2022) Towards critical white ice conditions in lakes under global warming. Nat Commun 13(1):4974. https://doi.org/10.1038/s41467-022-32633-1

Wu J, Gao X, Giorgi F, Chen D (2017) Changes of effective temperature and cold/hot days in late decades over China based on a high resolution gridded observation dataset. Intl J Climatol 37(S1):788–800. https://doi.org/10.1002/joc.5038

Wu J, Gao XJ (2013) A gridded daily observation dataset over China region and comparison with the other datasets (in Chinese). Chin J Geophysics 56(4):1102–1111. https://doi.org/10.6038/cjg20130406

Wu X, Wang X, Liu S, Yang Y, Xu G, Xu Y, Jiang T, Xiao C (2021) Snow cover loss compounding the future economic vulnerability of western China. Sci Total Environ 755:143025. https://doi.org/10.1016/j.scitotenv.2020.143025

Wu Z, Huang NE (2009) Ensemble empirical mode decomposition: a noise-assisted data analysis method, advances in adaptive data analysis. Adv Adapt Data Anal 1(1):1–41. https://doi.org/10.1142/S1793536909000047

Wu Z, Schneider EK, Kirtman BP, Sarachik ES, Huang NE, Tucker CJ (2008) The modulated annual cycle: an alternative reference frame for climate anomalies. Clim Dynam 31(7–8):823–841. https://doi.org/10.1007/s00382-008-0437-z

Xu B, Cao J, Hansen J, Yao T, Joswia DR, Wang N, Wu G, Wang M, Zhao H, Yang W, Liu X, He J (2009) Black soot and the survival of Tibetan glaciers. Proc Natl Acad Sci USA 106(52):22114–22118. https://doi.org/10.1073/pnas.0910444106

Yang Y, Chen R, Liu G, Liu Z, Wang X (2022) Trends and variability in snowmelt in China under climate change. Hydrol Earth Syst Sci 26(2):305–329. https://doi.org/10.5194/hess-26-305-2022

Zhang X, Zwiers FW, Hegerl GC, Hugo Lambert F, Gillett NP, Solomon S, Stott PA, Nozawa T (2007) Detection of human influence on twentieth-century precipitation trends. Nature 448(7152):461–465. https://doi.org/10.1038/nature06025

Zhao GP, Wang YX, Fan ZW, Ji Y, Liu M, Zhang W H, Li XL, Zhou SX, Li H, Liang S, Liu W, Yang Y, Fang LQ (2021) Mapping ticks and tick-borne pathogens in China. Nat Commun 12(1):1075. https://doi.org/10.1038/s41467-021-21375-1

Zheng H, Kang S, Chen P, Li Q, Tripathee L, Maharjan L, Guo J, Zhang Q, Santos E (2020) Sources and spatio-temporal distribution of aerosol polycyclic aromatic hydrocarbons throughout the Tibetan Plateau. Environ Pollut 261:114144. https://doi.org/10.1016/j.envpol.2020.114144

Zhu P, Burney J, Chang J, Jin Z, Mueller ND, Xin Q, Xu J, Yu L, Makowski D, Ciais P (2022) Warming reduces global agricultural production by decreasing cropping frequency and yields. Nat. Clim. Chang. 12(11):1016–1023. https://doi.org/10.1038/s41558-022-01492-5

Authors and Affiliations

Lihua Zhu[1] · Wei Hua[1] · Gang Huang[2,3] · Xin Lai[1]

✉ Wei Hua
huawei@cuit.edu.cn

[1] School of Atmospheric Sciences/Climate Change and Resource Utilization in Complex Terrain Regions Key Laboratory of Sichuan Province, Chengdu University of Information Technology, Chengdu 610225, China

[2] State Key Laboratory of Earth System Numerical Modeling and Application, Institute of Atmospheric Physics, Chinese Academy of Sciences, Beijing 100029, China

[3] University of Chinese Academy of Sciences, Beijing 100049, China